

# Integrated silicon photonic filters based on nanowire cascaded Sagnac loop resonators

David Moss (✉ [dmos@swin.edu.au](mailto:dmos@swin.edu.au))  
Swinburne University of Technology

---

## Research Article

**Keywords:** silicon photonics, nanowires, sagnac interferometers, optical filters

**Posted Date:** October 21st, 2021

**DOI:** <https://doi.org/10.21203/rs.3.rs-1001792/v1>

**License:**  This work is licensed under a Creative Commons Attribution 4.0 International License.

[Read Full License](#)

---

# Abstract

We demonstrate advanced integrated photonic filters in silicon-on-insulator (SOI) nanowires implemented by cascaded Sagnac loop reflector (CSLR) resonators. We investigate mode splitting in these standing-wave (SW) resonators and demonstrate its use for engineering the spectral profile of on-chip photonic filters. By changing the reflectivity of the Sagnac loop reflectors (SLRs) and the phase shifts along the connecting waveguides, we tailor mode splitting in the CSLR resonators to achieve a wide range of filter shapes for diverse applications including enhanced light trapping, flat-top filtering, Q factor enhancement, and signal reshaping. We present the theoretical designs and compare the CSLR resonators with three, four, and eight SLRs fabricated in SOI. We achieve versatile filter shapes in the measured transmission spectra via diverse mode splitting that agree well with theory. This work confirms the effectiveness of using CSLR resonators as integrated multi-functional SW filters for flexible spectral engineering.

## I. Introduction

Integrated photonic resonators have attracted great interest for their applications in signal modulation, buffering, switching, and processing in optical communications systems.<sup>1,2</sup> They have been enabled by advanced micro/nano fabrication technologies and offer compact footprints, mass producibility, scalability, and versatile filtering properties. Mode splitting induced by coherent optical mode interference in coupled resonant cavities is a key phenomenon in photonic resonators that can lead to powerful and versatile filtering functions such as optical analogues to electromagnetically-induced-transparency (EIT), Fano resonances, Autler-Townes splitting, and dark states.<sup>3-5</sup> It is similar in principle to atomic resonance splitting caused by quantum interference between excitation pathways in multi-level atomic systems.<sup>6</sup> One great advantage of this effect is that it can break the dependence between quality factor, free spectral range (FSR), and physical cavity length.<sup>7-9</sup> Moreover, the resulting group delay response and mode interaction are useful for enhancing light-material interaction and dispersion engineering in nonlinear optics.<sup>10-14</sup>

Photonic resonators can be classified into two categories – travelling-wave (TW) resonators, exemplified by ring resonators, and standing-wave (SW) resonators represented by photonic crystal cavities, distributed feedback cavities, and Fabry-Pero (FP) cavities.<sup>3</sup> The majority of work on mode splitting in photonic resonators has been based on TW resonators<sup>15-19</sup> although some recent work has investigated device structures consisting of both TW and SW resonators.<sup>20-22</sup> Since TW resonators are almost twice as long as their SW counterparts for the same FSR,<sup>23</sup> SW resonators tend to attract more interest in terms of device footprint. In addition, unlike the nearly uniform field distribution in TW resonators, the spatially dependent field distribution in SW resonators is useful for the efficient excitation of laser emission and nonlinear optical effects.<sup>24-28</sup>

In this paper, we demonstrate advanced integrated photonic filters in silicon-on-insulator (SOI) nanowires by exploiting mode splitting in SW resonators formed by cascaded Sagnac loop reflectors (SLRs), which

we term cascaded SLR (CSLR) resonators. We show that this is a powerful approach for engineering the spectral profile of on-chip filters. The concept of CSLR resonators was proposed in Refs. 23 and 17, and experimental demonstrations of CSLR resonators with two SLRs were reported in Refs. 23 and 29. For CSLR resonators with more than two SLRs, mode splitting occurs due to coherent interference between the FP cavities formed by the different SLRs. Here, we provide a detailed theory of mode splitting in CSLR resonators for spectral engineering, and experimentally demonstrate CSLR resonators with up to eight SLRs in SOI based nanowires. By changing the reflectivity of the SLRs and the phase shifts along the connecting waveguides, mode splitting in the CSLR resonators can be tailored for diverse applications such as enhanced light trapping, flat-top filtering, Q factor enhancement, and signal reshaping. We achieve high performance and versatile filter shapes that correspond to diverse mode splitting conditions. The experimental results confirm the effectiveness of our approach towards realizing integrated multi-functional SW filters for flexible spectral engineering.

## II. Device Configuration And Operation Principle

Figure 1 illustrates the schematic configuration of the integrated CSLR resonator. It consists of  $N$  SLRs ( $SLR_1, SLR_2, \dots, SLR_N$ ) formed by a self-coupled nanowire waveguide loop. In the CSLR resonator, each SLR performs as a reflection/transmission element and contributes to the overall transmission spectra from port IN to port OUT in Fig. 1. Therefore, the cascaded SLRs with a periodic loop lattice show similar transmission characteristics to that of photonic crystals.<sup>17</sup> The two adjacent SLRs together with the connecting waveguide form a FP cavity, thereby  $N$  cascaded SLRs can also be regarded as  $N-1$  cascaded FP cavities ( $FPC_1, FPC_2, \dots, FPC_{N-1}$ ), similar to Bragg gratings.<sup>30,31</sup> To study the CSLR resonator based on the scattering matrix method,<sup>32-33</sup> we define the waveguide and coupler parameters of the CSLR resonator in Table I, and so the field transmission function from port IN to port OUT can be written as:

$$T_{\text{CSLR}}(N) = \begin{cases} \frac{T_{s1}T_{s2}T_1}{1-R_{s1}R_{s2}T_1^2}, & N = 2 \\ \frac{T_{\text{CSLR}}(N-1)T_{sN}T_{N-1}}{1-R_{\text{CSLR}}(N-1)R_{sN}T_{N-1}^2}, & N > 2 \end{cases} \quad (1)$$

TABLE I. Definitions of waveguide and coupler parameters of the CSLR resonator

Waveguide	Length	Transmission factor <sup>a</sup>	Phase shift <sup>b</sup>
waveguide connecting SLR <sub><i>i</i></sub> to SLR <sub><i>i</i>+1</sub> ( <i>i</i> = 1, 2, ..., <i>N</i> -1)	<i>L<sub>i</sub></i>	<i>a<sub>i</sub></i>	$\varphi_i$
Sagnac loops in SLR <sub><i>i</i></sub> ( <i>i</i> = 1, 2, ..., <i>N</i> )	<i>L<sub>si</sub></i>	<i>a<sub>si</sub></i>	$\varphi_{si}$
Coupler	Coupling length <sup>c</sup>	Field transmission coefficient <sup>d</sup>	Field cross-coupling coefficient <sup>d</sup>
couplers in SLR <sub><i>i</i></sub> ( <i>i</i> = 1, 2, ..., <i>N</i> )	<i>L<sub>ci</sub></i>	<i>t<sub>i</sub></i>	<i>κ<sub>i</sub></i>

<sup>a</sup>  $a_i = \exp(-aL_i/2)$ ,  $a_{si} = \exp(-aL_{si}/2)$ , *a* is the power propagation loss factor.

<sup>b</sup>  $\varphi_i = 2\pi n_g L_i / \lambda$ ,  $\varphi_{si} = 2\pi n_g L_{si} / \lambda$ , *n<sub>g</sub>* is the group index and  $\lambda$  is the wavelength.

<sup>c</sup>  $L_{ci}$  (*i* = 1, 2, ..., *N*) are the straight coupling lengths shown in Fig.1. They are included in  $L_i$ .

<sup>d</sup> In our calculation, we assume  $t_i^2 + \kappa_i^2 = 1$  for lossless coupling in all the directional couplers.

In Eq. (1),  $T_{si}$  and  $R_{si}$  (*i* = 1, 2, ..., *N*) denote the field transmission and reflection functions of SLR<sub>*i*</sub> given by:

$$T_{si} = (t_i^2 - \kappa_i^2) a_{si} e^{-j\varphi_{si}}, \quad i = 1, 2, \dots, N \quad (2)$$

$$R_{si} = 2jt_i \kappa_i a_{si} e^{-j\varphi_{si}}, \quad i = 1, 2, \dots, N \quad (3)$$

$T_i$  (*i* = 1, 2, ..., *N*-1) represent the field transmission functions of the waveguide connecting SLR<sub>*i*</sub> to SLR<sub>*i*+1</sub>, which can be expressed as:

$$T_i = a_i e^{-j\varphi_i}, \quad i = 1, 2, \dots, N-1 \quad (4)$$

For the CSLR resonators implemented by SLR<sub>1</sub>, SLR<sub>2</sub>, ..., and SLR<sub>*i*</sub> (*i* = 1, 2, ..., *N*),  $T_{\text{CSLR}}(i)$  are the field transmission functions,  $R_{\text{CSLR}+}(i)$  and  $R_{\text{CSLR}-}(i)$  are the field reflection functions for light input from left and right sides, respectively, which can be given by:

$$R_{\text{CSLR-}}(i) = \begin{cases} \frac{R_{s2} + (T_{s2}^2 - R_{s2}^2)T_1^2 R_{s1}}{1 - R_{s1}R_{s2}T_1^2}, & i = 2 \\ \frac{R_{si} + (T_{si}^2 - R_{si}^2)T_{i-1}^2 R_{\text{CSLR-}}(i-1)}{1 - R_{\text{CSLR-}}(i-1)R_{si}T_{i-1}^2}, & i > 2 \end{cases} \quad (5)$$

$$R_{\text{CSLR+}}(i) = \begin{cases} \frac{R_{s1} + (T_{s1}^2 - R_{s1}^2)T_1^2 R_{s2}}{1 - R_{s1}R_{s2}T_1^2}, & i = 2 \\ \frac{R_{\text{CSLR+}}(i-1) + [T_{\text{CSLR}}(i-1)^2 - R_{\text{CSLR+}}(i-1)R_{\text{CSLR-}}(i-1)]T_{i-1}^2 R_{si}}{1 - R_{\text{CSLR-}}(i-1)R_{si}T_{i-1}^2}, & i > 2 \end{cases} \quad (6)$$

In Eqs. (2) and (3), it can be seen that the transmittance and reflectivity of the  $\text{SLR}_i$  depend on the  $t_i$ . In terms of practical fabrication, the  $t_i$  can be engineered by changing the coupling length  $L_{c_i}$ . The large dynamic range in the transmittance and reflectivity of individual SLRs that can be engineered by changing  $t_i$  or  $\kappa_i$  makes the CSLR resonator more flexible for spectral engineering as compared with Bragg gratings. On the other hand, according to Eq. (4), the transmission spectra of the CSLR resonators can also be tailored by changing  $\varphi_i$  ( $i = 1, 2, \dots, N-1$ ) - i.e., the phase shifts along the connecting waveguides. The freedom in designing  $t_i$  ( $i = 1, 2, \dots, N$ ) and  $\varphi_i$  ( $i = 1, 2, \dots, N-1$ ) is the basis for flexible spectral engineering based on the CSLR resonators, which can lead to versatile applications. In Eqs. (5) and (6),  $R_{\text{CSLR+}}(i)$  equals to  $R_{\text{CSLR-}}(i)$  only when  $\text{SLR}_1, \text{SLR}_2, \dots$ , and  $\text{SLR}_i$  are identical, i.e., when  $\text{SLR}_1, \text{SLR}_2, \dots$ , and  $\text{SLR}_i$  are not identical, there are nonreciprocal reflections from the CSLR resonators for light input from different directions. These non-reciprocal reflections are induced by different losses within the resonant cavity - the CSLR resonators themselves will still have reciprocal transmission for light input from different directions.

CSLR resonators with two SLRs ( $N = 2$ ) can be regarded as single FP cavities without mode splitting.<sup>23,29</sup> Here, we start from the CSLR resonators with three SLRs ( $N = 3$ ). Based on Eqs. (1) – (6), the calculated power transmission spectra and group delay spectra of the CSLR resonators with three SLRs ( $N = 3$ ) are depicted in Fig. 2. The structural parameters are chosen as follows:  $L_{s1} = L_{s2} = L_{s3} = 129.66 \mu\text{m}$ , and  $L_1 = L_2 = 100 \mu\text{m}$ . For single-mode silicon photonic nanowire waveguides with a cross-section of  $500 \text{ nm} \times 260 \text{ nm}$ , we use values based on our previously fabricated devices for the waveguide group index of the transverse electric (TE) mode ( $n_g = 4.3350$ ) and the propagation loss ( $\alpha = 55 \text{ m}^{-1}$  (2.4 dB/cm)). The same values of  $n_g$  and  $\alpha$  are also used for the calculations of other transmission and group delay spectra in this section. The calculated power transmission spectra of the CSLR resonator ( $N = 3$ ) for various  $t_2$  when  $t_1 = t_3 = 0.87$  are shown in Fig. 2(a). The corresponding group delay spectra are shown in Fig. 2(b). It is clear that different degrees of mode splitting can be achieved by varying  $t_2$ . As  $t_2$  decreases (i.e., the coupling strength increases), the spectral range between the two adjacent resonant peaks decreases until the split peaks finally merge into one. By further decreasing  $t_2$ , the Q factor, extinction ratio, and group delay of the combined single resonance increases, together with an increase in the insertion loss. In particular, when  $t_2 = 0.77$ , a band-pass Butterworth filter<sup>34</sup> with a flat-top filter shape can be realized,

which is desirable for signal filtering in optical communications systems.<sup>35,36</sup> On the other hand, when  $t_2 = 0.742$ , the CSLR resonator exhibits a flat-top group delay spectrum, which can be used as a Bessel filter for optical buffering.<sup>37,38</sup> When  $t_2 = \sqrt{1/2}$ , SLR<sub>2</sub> works as a total reflector, and so there is null transmission for the CSLR resonator. The same goes for  $t_1 = \sqrt{1/2}$  or  $t_3 = \sqrt{1/2}$ . Figure 2(c) shows the calculated power transmission spectra of the CSLR resonator ( $N = 3$ ) for various  $t_1 = t_3$  when  $t_2 = 0.97$ . The group delay spectra are depicted in Fig. 2(d) accordingly. One can see that decreasing  $t_1$  and  $t_3$  (i.e., enhancing the coupling strengths) results in increased Q factor, extinction ratio, and group delay, at the expense of an increase in the insertion loss. The sharpening of the filter shape can be attributed to coherent interference within the coupled resonant cavities, which could be useful for implementation of high-Q filters.<sup>7,32</sup>

Figure 3 shows the calculated power transmission spectra of asymmetric CSLR resonators ( $N = 3$ ) when  $L_1 \neq L_2$ . For comparison, we use the same field transmission coefficients  $[t_1, t_2, t_3] = [0.87, 0.77, 0.87]$  in the calculation. In Fig. 3(a), we plot the calculated power transmission spectra around one resonance when there are relatively small differences between  $L_1$  and  $L_2$ . It can be seen that the differences between  $L_1$  and  $L_2$  lead to different filter shapes of the CSLR resonator. In particular, when  $L_2 = 100.18 \mu\text{m}$ , the transmission spectrum of the CSLR resonator is almost the same as when  $L_2 = 100.00 \mu\text{m}$ . This is because in such a condition the difference between the phase along  $L_1$  and  $L_2$  is approximately  $\pi$ . Considering that the physical cavity length is half of the effective cavity length for a SW resonator,<sup>23</sup> the effective phase difference is about  $2\pi$ , and so there are almost the same transmission spectra resulting from coherent interference within in the resonant cavity. The calculated power transmission spectra in Fig. 3(a) also indicate that the filter shape of the CSLR resonator can be tuned or optimized by introducing thermo-optic micro-heaters<sup>19,33</sup> or carrier-injection electrodes<sup>39,40</sup> along  $L_{1,2}$  to tune the phase shift. Figure 3(b) presents the calculated power transmission spectra when there are relatively large differences between  $L_1$  and  $L_2$ . Due to the Vernier-like effect between the FPC<sub>1</sub> and FPC<sub>2</sub>, diverse mode splitting filter shapes are achieved at different resonances of the transmission spectra, which can be utilized to select resonances with desired filter shapes for passive photonic devices.<sup>41</sup> Such differences in the filter shapes become more obvious for an increased difference between  $L_1$  and  $L_2$ . In Fig. 3(c), we plot the calculated power transmission spectra when  $L_1 = 0$  and  $L_2 = mL_{s1}$  ( $m = 1, 2, 3, 4$ ). Since the effective cavity length of FPC<sub>*i*</sub> equals to  $L_{s*i*} + 2L_i + L_{s*i+1}}*$  ( $i = 1, 2$ ),<sup>23</sup> the various sets of  $L_1$  and  $L_2$  in Fig. 3(c) correspond to the conditions that the effective cavity length of FPC<sub>2</sub> is integer multiples of that of FPC<sub>1</sub>. We can see that there are split resonances with different numbers of transmission peaks in the spectra. Unlike the split resonances in Fig. 3(b), there are identical filter shapes in each period.

Figure 4 shows the calculated power transmission spectra of the CSLR resonators with four SLRs ( $N = 4$ ). In the calculation, we assume  $L_{s1} = L_{s2} = L_{s3} = L_{s4} = 129.66 \mu\text{m}$ , and  $L_1 = L_2 = L_3 = 100 \mu\text{m}$ . To simplify the comparison, we only show plots for the conditions that  $t_1 = t_4$ ,  $t_2 = t_3$  (Figs. 4(a) and (b)) and  $t_1 = t_3$ ,  $t_2 = t_4$  (Figs. 4(c) and (d)). The calculated power transmission spectra for various  $t_2 = t_3$  when  $t_1 = t_4 = 0.87$  are

shown in Fig. 4(a). The corresponding group delay spectra are provided in Fig. 4(b). It can be seen that the three split resonant peaks gradually merge to a single one as  $t_2$  and  $t_3$  decrease (i.e., the coupling strengths increase). After that, by further decreasing  $t_2$  and  $t_3$ , the Q factor, extinction ratio, and group delay of the combined single resonance increase, together with an increase in the insertion loss. This trend is similar to that in Figs. 3(a) and (b) for  $N = 3$ . Figure 4(c) depicts the calculated power transmission spectra for various  $t_2 = t_4$  when  $t_1 = t_3 = 0.85$ . The calculated group delay spectra are shown in Fig. 4(d) accordingly. For this condition, the CSLR resonator is no longer axisymmetric, and so the trend in Figs. 4(c) and (d) is different from that in Figs. 4(a) and (b). As  $t_2$  and  $t_4$  decrease (i.e., the coupling strengths increase), the transmission peak in the centre starts to appear and then becomes more pronounced, together with a decreased spectral range between the resonant peaks on both sides.

Figure 5(a) shows the calculated power transmission spectra of the CSLR resonators with different numbers of SLRs ( $N$ ). In the calculation, we use SLRs and connecting waveguides with the same lengths as those in Figs. 2 and 4. We also assume that  $t_1 = t_2 = \dots = t_N = 0.85$ . It can be seen that as  $N$  increases, the number of split resonances within one FSR also increases. For a CSLR resonator consisting of  $N$  SLRs, the maximum number of split resonances within one FSR is  $N-1$ . The differences between the maximum transmission of different resonant peaks are determined by the waveguide propagation loss, and these can be mitigated by decreasing the waveguide propagation loss ( $\alpha$ ) to the point where, in the limit of zero loss, they would no longer exist. In Fig. 5(b), we plot the calculated power transmission spectra of the CSLR resonator ( $N = 8$ ) for different  $t_1 = t_2 = \dots = t_8$ . As  $t_i$  ( $i = 1, 2, \dots, 8$ ) increases (i.e., the coupling strengths decrease), the bandwidth of the passband also increases, together with a decrease in insertion loss. In principle, the bandwidth of the passband is limited by the FSR of the CSLR resonator. Figures 5(c) – (f) show three specific optical filters designed based on the CSLR resonators with eight SLRs ( $N = 8$ ). The filter in Figs. 5(c) and (d) is designed for enhanced light trapping by introducing an additional  $\pi/2$  phase shift along the centre FPC (i.e.,  $L_4$  for  $N = 8$ ), which is similar to enhancing light trapping in photonic crystals by introducing defects.<sup>17</sup> In the calculation, we assume that  $t_1 = t_2 = \dots = t_8 = 0.97$ . With enhanced light trapping, there are increased time delays and enhanced light-matter interactions, which are useful in nonlinear optics and laser excitation.<sup>10,11,27,28</sup> In Fig. 5(c), one can see that there are central transmission peaks induced by an additional phase shift along  $L_4$ , which correspond to a group delay 2.1 times higher than that of the CSLR resonator without the additional phase shift in Fig. 5(d). This group delay can be increased further by using more cascaded SLRs. The filter in Fig. 5(e) is an 8th-order Butterworth filter with a flat-top filter shape. The field transmission coefficients of  $SLR_j$  ( $j = 1, 2, \dots, 8$ ) are  $[t_1, t_2, t_3, t_4, t_5, t_6, t_7, t_8] = [0.98, 0.94, 0.91, 0.90, 0.90, 0.91, 0.94, 0.98]$ , respectively. Figure 5(f) shows the designed optical filter with multiple transmission peaks in the spectrum. Each transmission peak has a high extinction ratio of over 10 dB. The field transmission coefficients of  $SLR_j$  ( $j = 1, 2, \dots, 8$ ) in this filter are  $[t_1, t_2, t_3, t_4, t_5, t_6, t_7, t_8] = [0.84, 0.935, 0.945, 0.955, 0.955, 0.945, 0.935, 0.84]$ , respectively. By tailoring the transmission of individual resonant peaks via changing  $t_i$  and  $\varphi_i$ , these CSLR resonators could potentially find applications in RF spectral shaping and broadband arbitrary RF waveform generation<sup>42,43</sup>. Based on two-photon absorption (TPA)-induced free carrier

dispersion (FCD)<sup>44</sup>, CSLR resonators with multiple transmission peaks could also be used for wavelength multicasting in wavelength division multiplexing (WDM) systems.<sup>9,45</sup> It is also worth mentioning that the narrow bandwidth between the split resonances arises from coherent interference within the CSLR resonators. For ring resonators, such a narrow bandwidth can only be achieved by using much larger loop circumferences, thus leading to much larger device footprints. In addition, the CSLR resonator is a SW resonator, and so the cavity length is nearly half that of a TW resonator (e.g., ring resonator) with the same FSR, which enables even more compact device footprints.

## iii. Device Fabrication

We fabricated a series of CSLR filters based on the designs in Section II, on an SOI wafer with a 260-nm-thick top silicon layer and 3- $\mu\text{m}$ -thick buried oxide layer. The device fabrication involved standard complementary metal-oxide-semiconductor (CMOS) processes only, with the exception that the device pattern was defined using electron-beam lithography (EBL). The micrographs for the fabricated devices with four and eight SLRs are shown in Figs. 6(a) and (b), respectively. A zoom-in micrograph for the SLR is shown in Fig. 6(c). In our fabrication, EBL (Vistec EBPG 5200) was employed to define the device pattern on positive photoresist (ZEP520A), followed by a reactive ion etching (RIE) process to transfer the device layout to the top silicon layer of the SOI wafer. Grating couplers for TE polarization were employed at the ends of input and output ports to couple light into and out of the chip with single mode fibres, respectively. The grating couplers were fabricated by another EBL step, together with a second RIE process. Gold markers, prepared by metal lift-off after photolithography and electron beam evaporation, were employed for alignment between the two times EBL. A 1.5- $\mu\text{m}$ -thick silica layer is deposited by plasma enhanced chemical vapor deposition (PECVD) to cover the whole device as upper cladding. For all the devices, the width of the waveguides is 500 nm and the gap size of all the directional couplers was 100 nm. Different coupling strengths for different SLRs were achieved by changing  $L_{c_i}$  ( $i = 1, 2, \dots, N$ ) in Fig. 1. Compared with silicon waveguide Bragg gratings based on small physical corrugations, the fabrication of self-coupled nanowire waveguides doesn't require high lithography resolution and shows relatively high tolerance to fabrication imperfections such as lithographic smoothing effects and quantization errors due to the finite grid size.<sup>30</sup> For the calculations in Section II,  $L_{c_i}$  ( $i = 1, 2, \dots, N$ ) are included in  $L_j$  ( $j = 1, 2, \dots, N-1$ ). Their relation is given by:

$$L_i = L_i' + L_{c_i} + L_{c_{i+1}}, \quad i = 1, 2, \dots, N-1 \quad (7)$$

where  $L_i'$  ( $i = 1, 2, \dots, N-1$ ) are the lengths of the connecting waveguides excluding the straight coupling lengths. For practical fabrication, we used the same Sagnac loop structure for each SLR, with the differences in  $L_{c_i}$  ( $i = 1, 2, \dots, N$ ) compensated by slightly changing  $L_i'$  ( $i = 1, 2, \dots, N-1$ ) according to Eq. (7).

## Iv. Device Characterisation

The normalized transmission spectra for the fabricated CSLR resonators with three SLRs ( $N = 3$ ) are shown in Figs. 7(a) and (b) by the blue solid curves. The spectra were measured by sweeping a fast-scan continuous-wave (CW) laser (Keysight 81608A) with a power of  $\sim 0$  dBm. The output powers from the devices under test were recorded using a high-sensitivity optical power meter (Keysight N7744A). The measured transmission spectra are normalized and plot after excluding the losses caused by the grating couplers, which was  $\sim 6$  dB each, or  $\sim 12$  dB for both. The normalized spectra are then fit by the red dashed curves calculated based on Eqs. (1) – (6). The fit parameters are listed in Table II, which are close to our expectations from the design. For  $n_g$ ,  $\alpha$ , and  $t_i$ , the difference between the fit and designed values are smaller than 0.01,  $20 \text{ m}^{-1}$  (0.6 dB/cm), and 0.05, respectively. The residual differences between the fit  $n_g$  and  $\alpha$  can be attributed to slight variations between the fabricated samples. In Fig. 7(a), various mode splitting spectra of the fabricated devices with different  $L_{c2}$  are obtained, which are consistent with the theory in Fig. 2(a). The measured spectra of the fabricated devices with different  $L_{c1} = L_{c3}$  in Fig. 7(b) also agree well with the theory in Fig. 2(c). These experimental results verify that the transmission spectra of the CSLR resonators can be tailored by changing the coupling strengths of the directional couplers in the SLRs. Since we have demonstrated in Ref. 29 that dynamic tuning of the coupling strengths can be realized by using interferometric couplers to replace the directional couplers and tuning them in a differential mode, tuning of the transmission spectra of the CSLR resonators can also be achieved in the same way.

**TABLE II. Fit parameters of the measured transmission spectra in Figs. 7, 8, and 9**

Figure	Fit parameters
Fig. 7(a)	<ol style="list-style-type: none"> <li><math>n_g = 4.3202, \alpha = 62 \text{ m}^{-1}</math> (<math>\sim 2.7 \text{ dB/cm}</math>), <math>[t_1, t_2, t_3] = [0.876, 0.995, 0.876]</math></li> <li><math>n_g = 4.3221, \alpha = 64 \text{ m}^{-1}</math> (<math>\sim 2.8 \text{ dB/cm}</math>), <math>[t_1, t_2, t_3] = [0.883, 0.785, 0.883]</math></li> <li><math>n_g = 4.3220, \alpha = 64 \text{ m}^{-1}</math> (<math>\sim 2.8 \text{ dB/cm}</math>), <math>[t_1, t_2, t_3] = [0.886, 0.734, 0.886]</math></li> </ol>
Fig. 7(b)	<ol style="list-style-type: none"> <li><math>n_g = 4.3178, \alpha = 59 \text{ m}^{-1}</math> (<math>\sim 2.6 \text{ dB/cm}</math>), <math>[t_1, t_2, t_3] = [0.982, 0.975, 0.982]</math></li> <li><math>n_g = 4.3180, \alpha = 59 \text{ m}^{-1}</math> (<math>\sim 2.6 \text{ dB/cm}</math>), <math>[t_1, t_2, t_3] = [0.902, 0.976, 0.902]</math></li> <li><math>n_g = 4.3180, \alpha = 60 \text{ m}^{-1}</math> (<math>\sim 2.6 \text{ dB/cm}</math>), <math>[t_1, t_2, t_3] = [0.829, 0.974, 0.829]</math></li> </ol>
Fig. 8(a)	$L_2 = 100.0 \text{ }\mu\text{m}$ : $n_g = 4.3252, \alpha = 58 \text{ m}^{-1}$ ( $\sim 2.6 \text{ dB/cm}$ ), $[t_1, t_2, t_3] = [0.882, 0.788, 0.882]$ $L_2 = 107.2 \text{ }\mu\text{m}$ : $n_g = 4.3249, \alpha = 58 \text{ m}^{-1}$ ( $\sim 2.6 \text{ dB/cm}$ ), $[t_1, t_2, t_3] = [0.880, 0.789, 0.880]$
Fig. 8(b)	$L_2 = 259.33 \text{ }\mu\text{m}, n_g = 4.3252, \alpha = 64 \text{ m}^{-1}$ ( $\sim 2.8 \text{ dB/cm}$ ), $[t_1, t_2, t_3] = [0.882, 0.783, 0.882]$
Fig. 9(a)	<ol style="list-style-type: none"> <li><math>n_g = 4.3278, \alpha = 60 \text{ m}^{-1}</math> (<math>\sim 2.6 \text{ dB/cm}</math>), <math>[t_1, t_2, t_3, t_4] = [0.882, 0.992, 0.992, 0.882]</math></li> <li><math>n_g = 4.3280, \alpha = 58 \text{ m}^{-1}</math> (<math>\sim 2.6 \text{ dB/cm}</math>), <math>[t_1, t_2, t_3, t_4] = [0.931, 0.832, 0.832, 0.931]</math></li> <li><math>n_g = 4.3272, \alpha = 60 \text{ m}^{-1}</math> (<math>\sim 2.6 \text{ dB/cm}</math>), <math>[t_1, t_2, t_3, t_4] = [0.834, 0.958, 0.958, 0.834]</math></li> </ol>
Fig. 9(b)	$n_g = 4.3300, \alpha = 65 \text{ m}^{-1}$ ( $\sim 2.8 \text{ dB/cm}$ ), $L_4 = 100.09 \text{ }\mu\text{m}$ , $[t_1, t_2, t_3, t_4, t_5, t_6, t_7, t_8] = [0.962, 0.962, 0.962, 0.962, 0.962, 0.962, 0.962, 0.962]$
Fig. 9(c)	$n_g = 4.3288, \alpha = 68 \text{ m}^{-1}$ ( $\sim 3.0 \text{ dB/cm}$ ), $[t_1, t_2, t_3, t_4, t_5, t_6, t_7, t_8] = [0.998, 0.967, 0.942, 0.913, 0.913, 0.942, 0.967, 0.998]$
Fig. 9(d)	$n_g = 4.3299, \alpha = 64 \text{ m}^{-1}$ ( $\sim 2.8 \text{ dB/cm}$ ), $[t_1, t_2, t_3, t_4, t_5, t_6, t_7, t_8] = [0.874, 0.941, 0.972, 0.982, 0.982, 0.972, 0.941, 0.874]$

The measured and fit transmission spectra of the fabricated asymmetric CSLR resonator ( $N = 3$ ) with  $L_1 = 100.0 \text{ }\mu\text{m}$  and  $L_2 = 107.2 \text{ }\mu\text{m}$  are shown in Fig. 8(a). For comparison, the measured and fit transmission spectra of a symmetric CSLR resonator ( $N = 3$ ) with  $L_1 = L_2 = 100.0 \text{ }\mu\text{m}$  are also shown. The fit parameters are also given in Table II. For the symmetric CSLR resonator, there is negligible difference between the filter shapes of different resonances. In contrast, due to the Vernier-like effect, there are obvious differences between the filter shapes of different resonances for the fabricated asymmetric CSLR

resonator. These experimental results match with the theory in Fig. 3(b). Figure 8(b) shows the measured and fit transmission spectra of the fabricated asymmetric CSLR resonator ( $N = 3$ ) with  $L_1' = L_1 - L_{c1} - L_{c2} = 0$   $\mu\text{m}$  and  $L_2 = 295.33$   $\mu\text{m}$ . In the device pattern, the loop region of SLR<sub>1</sub> was rotated to the bottom side of SLR<sub>2</sub>. It can be seen that the measured spectrum shows good agreement with the theory in Fig. 3(c), with the discrepancies mainly arising from the grating coupler spectral response as well as slight variations in coupling coefficients with wavelength.<sup>46</sup> The dispersion of the SOI nanowire waveguides is another factor that could account for the discrepancies, since we used  $n_g$  rather than the wavelength-dependent effective index to match the FSR in our theoretical calculations.

The measured and fit transmission spectra of the fabricated CSLR resonators with four SLRs ( $N = 4$ ) are shown in Fig. 9(a). The fitting parameters are listed in Table II. One can see that diverse filter shapes are obtained for the fabricated devices with different coupling lengths, and all the measured spectra agree well with the theory in Fig. 4. Figures 9(b) – (d) show the measured and fit transmission spectra of the fabricated CSLR resonators with eight SLRs ( $N = 8$ ). The fitting parameters are also provided in Table II. The device in Fig. 8(b) was designed for enhanced light trapping, and the measured transmission spectrum is similar to the calculated spectrum in Fig. 5(c). The measured filter shape in Fig. 9(b) exhibits a slight asymmetry and this is because the additional phase shift along  $L_4$  is not exactly  $\pi/2$ . By introducing thermo-optic micro-heaters or carrier-injection electrodes along  $L_4$  to tune the phase shift, the symmetry of the filter shape can be improved further. The device in Fig. 9(c) was designed to perform as an 8th-order Butterworth filter with a flat-top filter shape. As can be seen, the passband is almost flat, which is close to the calculated spectrum in Fig. 5(e). The 3-dB bandwidth is  $\sim 0.7$  nm, which is significantly narrower than what can typically be achieved by silicon waveguide Bragg gratings<sup>30</sup>. By either increasing the relevant  $t_i$  or by increasing the number of SLRs, the 3-dB bandwidth can be further improved. The slight unevenness of the top of the transmission band can be attributed to discrepancies between the designed and practical coupling coefficients. Figure 9(d) shows the measured transmission spectrum with multiple resonant peaks. The minimum extinction ratio of the transmission peaks is  $\sim 7.8$  dB, which is slightly lower than that in Fig. 5(f). This is mainly because the waveguide propagation loss of the fabricated devices ( $\alpha = 64$   $\text{m}^{-1}$ ) is slightly higher than we assumed in the calculation ( $\alpha = 55$   $\text{m}^{-1}$ ). By further reducing the propagation loss, higher extinction ratios of the split resonances can be obtained.

These results are applicable to a wide range of optical platforms such as Hydex<sup>47–64</sup> and silicon nitride.<sup>65</sup> Further, these types of advanced filters would have interesting applications for nonlinear devices incorporating graphene and graphene oxide,<sup>66–75</sup> as well as advanced nonlinear devices such as microcomb nonlinear devices for applications to microwave photonics and other high bandwidth applications<sup>76–111</sup> and even mid infrared applications.<sup>112–118</sup>

## V. Conclusion

In summary, we design and fabricate sophisticated and high performance optical filters in SOI nanowires through the use of mode splitting in integrated CSLR resonators, by designing the reflectivity of the SLRs

and the phase shifts along the connecting waveguides. These filters are extremely useful for a wide range of applications including enhanced light trapping, flat-top filtering, Q factor enhancement, and signal reshaping. We theoretically analyse and practically fabricate devices with up to eight SLRs. We measure the transmission spectra of the fabricated devices and obtain versatile filter shapes corresponding to diverse mode splitting conditions. The experimental results are consistent with theory and validate the CSLR resonator as a powerful and versatile approach to realise multi-functional SW filters for flexible spectral engineering in photonic integrated circuits.

## Declarations

### Competing interests:

The authors declare no competing interests.

## References

1. W. Bogaerts, P. De Heyn, T. Van Vaerenbergh, K. De Vos, S. Selvaraja, T. Claes, P. Dumon, P. Bienstman, D. Van Thourhout, and R. Baets, *Laser Photon. Rev.* **6**, 47 (2012).
2. S. Feng, T. Lei, H. Chen, H. Cai, X. Luo, and A. W. Poon, *Laser Photon. Rev.* **6**, 145 (2012).
3. Q. Li, T. Wang, Y. Su, M. Yan, and M. Qiu, *Opt. Exp.* **18**, 8367 (2010).
4. B. Peng, ŞK Özdemir, W. Chen, F. Nori, and L. Yang, *Nat. Commun.* **5**, 1 (2014).
5. M. Limonov, M. Rybin, A. Poddubny, and Y. Kivshar, *Nat. Photon.* **11**, 543 (2017).
6. M. Fleischhauer, A. Imamoglu, J. P. Marangos, *Rev. Mod. Phys.* **77**, 633 (2005).
7. L. Barea, F. Vallini, G. de Rezende, and N. Frateschi, *Photon. J.* **5**, 2202717 (2013).
8. L. Barea, F. Vallini, P. Jarschel, and N. Frateschi, *App. Phys. Lett.* **103**, 201102 (2013).
9. M. Souza, L. Barea, F. Vallini, G. Rezende, G. Wiederhecker, and N. Frateschi, *Opt. Exp.* **22**, 10430 (2014).
10. M. D. Lukin and A. Imamoglu, *Nature* **413**, 273 (2001).
11. C. Monat, C. Grillet, B. Corcoran, D. J. Moss, B. J Eggleton, T. P. White, and T. F. Krauss, *Opt. Exp.* **18**, 6831 (2010).
12. X. Xue, Y. Xuan, P. Wang, Y. Liu, D. Leaird, M. Qi, and A. Weiner, *Laser Photon. Rev.* **9**, 123 (2015).
13. S. Kim, K. Han, C. Wang, J. Villegas, X. Xue, C. Bao, Y. Xuan, D. Leaird, A. Weiner, and M. Qi, *Nat. Commun.* **8**, 1 (2017).
14. M. Souza, G. Rezende, L. Barea, G. Wiederhecker, and N. Frateschi, *Opt. Exp.* **24**, 18960 (2016).
15. L. Zhang, M. Song, T. Wu, L. Zou, R. Beausoleil, and A. Willner, *Opt. Lett.* **33**, 1978 (2008).
16. L. Zhou, T. Ye, and J. Chen, *Opt. Lett.* **36**, 13 (2011).
17. J. Song, L. Luo, X. Luo, H. Zhou, X. Tu, L. Jia, Q. Fang, and G. Lo, *Opt. Exp.* **22**, 24202 (2014).
18. J. Wu, B. Liu, J. Peng, J. Mao, X. Jiang, C. Qiu, C. Tremblay, and Y. Su, *J. Lightw. Technol.* **33**, 3542 (2015).

19. M. Souza, G. Rezende, L. Barea, A. Zuben, G. Wiederhecker, and N. Frateschi, *Opt. Lett.* **40**, 3332 (2015).
20. A. Li and W. Bogaerts, *Opt. Exp.* **25**, 31688 (2017).
21. A. Li and W. Bogaerts, *APL Photonics* **2**, 096101 (2017).
22. S. Zheng, Z. Ruan, S. Gao, Y. Long, S. Li, M. He, N. Zhou, J. Du, L. Shen, X. Cai and J. Wang, *Opt. Exp.* **25**, 25655 (2017).
23. X. Sun, L. Zhou, J. Xie, Z. Zou, L. Lu, H. Zhu, X. Li, and J. Chen, *Opt. Lett.* **38**, 567 (2013).
24. Y. Ni, *App. Opt.* **19**, 3425 (1980).
25. V. Van, *Optical Microring Resonators: Theory, Techniques, and Applications*, CRC Press, 2016), p.53.
26. Z. Wang, B. Tian, M. Pantouvaki, W. Guo, P. Absil, J. Van Campenhout, C. Merckling, and D. Van Thourhout, *Nat. Photon.* **9**, 837 (2015).
27. S. Wu, S. Buckley, J. Schaibley, L. Feng, J. Yan, D. Mandrus, F. Hatami, W. Yao, J. Vučković, A. Majumdar, and X. Xu, *Nature* **520**, 69 (2015).
28. T. Gu, N. Petrone, J. McMillan, A. van der Zande, M. Yu, G. Lo, D. Kwong, J. Hone, and C. Wong, *Nat. Photon.* **6**, 554 (2012).
29. X. Jiang, J. Wu, Y. Yang, T. Pan, J. Mao, B. Liu, R. Liu, Y. Zhang, C. Qiu, C. Tremblay, and Y. Su, *Opt. Exp.* **24**, 2183 (2016).
30. X. Wang, Y. Wang, J. Flueckiger, R. Bojko, A. Liu, A. Reid, J. Pond, N. Jaeger, and L. Chrostowski, *Opt. Lett.* **39**, 5519 (2014).
31. L. Lu, F. Li, M. Xu, T. Wang, J. Wu, L. Zhou, and Y. Su, *Photon. Technol. Lett.* **24**, 1765 (2012).
32. J. Wu, T. Moein, X. Xu, G. Ren, A. Mitchell, and D. J. Moss, *APL Photonics* **2**, 056103 (2017)
33. J. Wu, P. Cao, T. Pan, Y. Yang, C. Qiu, C. Tremblay, and Y. Su, *Photon. Res.* **3**, 9 (2015).
34. H. Liu and A. Yariv, *Opt. Exp.* **19**, 17653 (2011).
35. B. Little, S. Chu, P. Absil, J. Hryniewicz, F. Johnson, F. Seiferth, D. Gill, V. Van, O. King, and M. Trakalo, *Photon. Technol. Lett.* **16**, 2263 (2004).
36. F. Xia, M. Rooks, L. Sekaric, and Y. Vlasov, *Opt. Exp.* **15**, 11934 (2007).
37. F. Xia, L. Sekaric, Y. Vlasov, *Nat. Photon.* **1**, 65 (2007).
38. J. Poon, J. Scheuer, Y. Xu, and A. Yariv, *J. Opt. Soc. Am. B*, **21**, 1665 (2004).
39. L. Zhou and A. W. Poon, *Opt. Exp.* **15**, 9194 (2007).
40. J. Wu, P. Cao, X. Hu, X. Jiang, T. Pan, Y. Yang, C. Qiu, C. Tremblay, Y. Su, *Opt. Exp.* **22**, 26254 (2014).
41. J. Wu, P. Cao, X. Hu, T. Wang, M. Xu, X. Jiang, F. Li, L. Zhou, and Y. Su, *Photon. Technol. Lett.* **25**, 580 (2013).
42. M. Khan, H. Shen, Y. Xuan, L. Zhao, S. Xiao, D. Leaird, A. Weiner, and M. Qi, *Nat. Photon.* **4**, 117 (2010).

43. J. Wang, H. Shen, L. Fan, R. Wu, B. Niu, L. Varghese, Y. Xuan, D. Leaird, X. Wang, F. Gan, A. Weiner, and M. Qi, *Nat. Commun.* **6**, 1 (2015).
44. J. Wu, X. Jiang, T. Pan, P. Cao, L. Zhang, X. Hu, Y. Su, *Chi. Sci. Bull.* **59**, 2702 (2014).
45. Q. Li, Z. Zhang, F. Liu, M. Qiu, and Y. Su, *App. Phys. Lett.* **93**, 081113 (2008).
46. Q. Chen, Y. Yang, and Y. Huang, *App. Phys. Lett.* **89**, 061118 (2006).
47. D. J. Moss, R. Morandotti, A. L. Gaeta, and M. Lipson, "New CMOS-compatible platforms based on silicon nitride and Hydex for nonlinear optics," *Nature Photonics*, vol. 7, no. 8, pp. 597–607, 2013.
48. M. Ferrera, L. Razzari, D. Duchesne, R. Morandotti, Z. Yang, M. Liscidini, J. E. Sipe, S. Chu, B. E. Little, and D. J. Moss, "Low-power continuous-wave nonlinear optics in doped silica glass integrated waveguide structures," *Nature Photonics*, vol. 2, no. 12, pp. 737–740, 2008/12/01, 2008.
49. L. Razzari, D. Duchesne, M. Ferrera, R. Morandotti, S. Chu, B. E. Little, and D. J. Moss, "CMOS-compatible integrated optical hyper-parametric oscillator," *Nature Photonics*, vol. 4, no. 1, pp. 41–45, 2010/01/01, 2010.
50. B. Corcoran, C. Monat, C. Grillet, D. J. Moss, B. J. Eggleton, T. P. White, L. O'Faolain, and T. F. Krauss, "Green light emission in silicon through slow-light enhanced third-harmonic generation in photonic-crystal waveguides," *Nature Photonics*, vol. 3, no. 4, pp. 206-210, 2009/04/01, 2009.
51. A. Pasquazi, M. Peccianti, Y. Park, B. E. Little, S. T. Chu, R. Morandotti, J. Azaña, and D. J. Moss, "Sub-picosecond phase-sensitive optical pulse characterization on a chip," *Nature Photonics*, vol. 5, no. 10, pp. 618-623, 2011/10/01, 2011.
52. H. Bao, et al., "Laser cavity-soliton microcombs", *Nature Photonics*, vol. 13, no. 6, pp. 384-389, Jun. 2019.
53. M. Ferrera et al., "CMOS compatible integrated all-optical radio frequency spectrum analyzer", *Optics Express*, vol. 22, no. 18, pp. 21488–21498 (2014).
54. M. Kues, et al., "Passively modelocked laser with an ultra-narrow spectral width", *Nature Photonics*, vol. 11, no. 3, pp. 159, 2017.
55. M. Ferrera et al., "On-Chip ultra-fast 1st and 2nd order CMOS compatible all-optical integration", *Optics Express*, vol. 19, no. 23, pp. 23153–23161 (2011).
56. D. Duchesne, M. Peccianti, M. R. E. Lamont, et al., "Supercontinuum generation in a high index doped silica glass spiral waveguide," *Optics Express*, vol. 18, no. 2, pp. 923–930, 2010.
57. M. Ferrera, et al., "On-chip CMOS-compatible all-optical integrator", *Nature Communications*, vol. 1, Article 29, 2010. DOI:10.1038/ncomms1028
58. A. Pasquazi, et al., "All-optical wavelength conversion in an integrated ring resonator," *Optics Express*, vol. 18, no. 4, pp. 3858–3863, 2010.
59. A. Pasquazi, Y. Park, J. Azana, et al., "Efficient wavelength conversion and net parametric gain via Four Wave Mixing in a high index doped silica waveguide," *Optics Express*, vol. 18, no. 8, pp. 7634–7641, 2010.

60. M. Peccianti, M. Ferrera, L. Razzari, et al., "Subpicosecond optical pulse compression via an integrated nonlinear chirper," *Optics Express*, vol. 18, no. 8, pp. 7625–7633, 2010.
61. M. Ferrera et al., "Low Power CW Parametric Mixing in a Low Dispersion High Index Doped Silica Glass Micro-Ring Resonator with Q-factor > 1 Million", *Optics Express*, vol.17, no. 16, pp. 14098–14103 (2009).
62. M. Peccianti, et al., "Demonstration of an ultrafast nonlinear microcavity modelocked laser", *Nature Communications*, vol. 3, pp. 765, 2012. DOI:10.1038/ncomms1762
63. A. Pasquazi, L. Caspani, M. Peccianti, et al., "Self-locked optical parametric oscillation in a CMOS compatible microring resonator: a route to robust optical frequency comb generation on a chip," *Optics Express*, vol. 21, no. 11, pp. 13333–13341, 2013.
64. A. Pasquazi, M. Peccianti, B. E. Little, et al., "Stable, dual mode, high repetition rate mode-locked laser based on a microring resonator," *Optics Express*, vol. 20, no. 24, pp. 27355–27362, 2012.
65. A. Frigg, A. Boes, G. Ren, T.G. Nguyen, D.Y. Choi, S. Gees, D. Moss, A. Mitchell, "Optical frequency comb generation with low temperature reactive sputtered silicon nitride waveguides", *APL Photonics*, vol.5, Issue 1, 011302 (2020).
66. J. Wu, L. Jia, Y. Zhang, Y. Qu, B. Jia, and D. J. Moss, "Graphene oxide for integrated photonics and flat optics," *Advanced Materials*, vol. 32, 2006415, pp.1–29, 2020.
67. Y. Yang, H. Lin, B. Y. Zhang, Y. Zhang, X. Zheng, A. Yu, M. Hong, and B. Jia, "Graphene-based multilayered metamaterials with phototunable architecture for on-chip photonic devices," *ACS Photonics*, vol. 6, no. 4, pp. 1033–1040, 2019/04/17, 2019.
68. Y. Yang, J. Wu, X. Xu, Y. Liang, S. T. Chu, B. E. Little, R. Morandotti, B. Jia, and D. J. Moss, "Invited Article: Enhanced four-wave mixing in waveguides integrated with graphene oxide," *APL Photonics*, vol. 3, no. 12, pp. 120803, 2018/12/01, 2018.
69. J. Wu, Y. Yang, Y. Qu, L. Jia, Y. Zhang, X. Xu, S. T. Chu, B. E. Little, R. Morandotti, B. Jia, and D. J. Moss, "2D layered graphene oxide films integrated with micro-ring resonators for enhanced nonlinear optics," *Small*, vol. 16, no. 16, pp. 1906563, 2020/04/01, 2020.
70. Y. Zhang, J. Wu, Y. Yang, Y. Qu, L. Jia, T. Moein, B. Jia, and D. J. Moss, "Enhanced Kerr nonlinearity and nonlinear figure of merit in silicon nanowires integrated with 2D graphene oxide films," *ACS Applied Materials & Interfaces*, vol. 12, no. 29, pp. 33094-33103, 2020/07/22, 2020.
71. Y. Qu, J. Wu, Y. Yang, Y. Zhang, Y. Liang, H. El Dirani, R. Crochemore, P. Demongodin, C. Sciancalepore, C. Grillet, C. Monat, B. Jia, and D. J. Moss, "Enhanced four-wave mixing in silicon nitride waveguides integrated with 2D layered graphene oxide films," *Advanced Optical Materials*, Vol. 8, No. 21, 2001048, 2020/10/19, 2020.
72. J. Wu, Y. Yang, Y. Qu, X. Xu, Y. Liang, S. T. Chu, B. E. Little, R. Morandotti, B. Jia, and D. J. Moss, "Graphene oxide waveguide and micro-ring resonator polarizers," *Laser & Photonics Reviews*, vol. 13, no. 9, pp. 1900056, 2019/09/01, 2019.
73. Y. Qu, J. Wu, Y. Zhang, Y. Liang, B. Jia, and D.J. Moss, "Analysis of four-wave mixing in silicon nitride waveguides integrated with 2D layered graphene oxide films", *Journal of Lightwave Technology*,

- Vol. 39, Early Access (2021). DOI: 10.1109/JLT.2021.3059721.
74. T. Moein et al., "Optically-Thin Broadband Graphene-Membrane Photodetector", *Nanomaterials*, vol. 10, issue 3, 407 (2020).
75. Yuning Zhang, Jiayang Wu, Yang Qu, Linnan Jia, Baohua Jia, and David J. Moss, "Optimizing the Kerr nonlinear optical performance of silicon waveguides integrated with 2D graphene oxide films", *Journal of Lightwave Technology*, Vol. 39, Early Access (2021). DOI: 10.1109/JLT.2021.3069733.
76. Mengxi Tan, X. Xu, J. Wu, T. G. Nguyen, S. T. Chu, B. E. Little, R. Morandotti, A. Mitchell, and David J. Moss, "Photonic Radio Frequency Channelizers based on Kerr Optical Micro-combs", *Journal of Semiconductors* (background-color:#FFCC66;buvertical-align:super;>42</background-color:#FFCC66;buvertical-align:super;> (4), 041302 (2021). (ISSN 1674–4926). DOI:10.1088/1674-4926/42/4/041302.
77. H.Bao, L.Olivieri, M.Rowley, S.T. Chu, B.E. Little, R.Morandotti, D.J. Moss, J.S.T. Gongora, M.Peccianti and A.Pasquazi, "Laser Cavity Solitons and Turing Patterns in Microresonator Filtered Lasers: properties and perspectives", Paper No. LA203-5, Paper No. 11672-5, SPIE LASE, SPIE Photonics West, San Francisco CA March 6-11 (2021). DOI:10.1117/12.2576645
78. Mengxi Tan, X. Xu, J. Wu, A. Boes, T. G. Nguyen, S. T. Chu, B. E. Little, R. Morandotti, A. Mitchell, and David J. Moss, "Advanced microwave signal generation and processing with soliton crystal microcombs", or "Photonic convolutional accelerator and neural network in the Tera-OPs regime based on Kerr microcombs", Paper No. **11689-38**, PW210-OE201-67, Integrated Optics: Devices, Materials, and Technologies XXV, SPIE Photonics West, San Francisco CA March 6-11 (2021). DOI: 10.1117/12.2584017
79. Mengxi Tan, Bill Corcoran, Xingyuan Xu, Andrew Boes, Jiayang Wu, Thach Nguyen, Sai T. Chu, Brent E. Little, Roberto Morandotti, Arnan Mitchell, and David J. Moss, "Optical data transmission at 40 Terabits/s with a Kerr soliton crystal microcomb", Paper No.11713-8, PW210-OE803-23, Next-Generation Optical Communication: Components, Sub-Systems, and Systems X, SPIE Photonics West, San Francisco CA March 6-11 (2021). DOI:10.1117/12.2584014
80. Mengxi Tan, X. Xu, J. Wu, A. Boes, T. G. Nguyen, S. T. Chu, B. E. Little, R. Morandotti, A. Mitchell, and David J. Moss, "RF and microwave photonic, fractional differentiation, integration, and Hilbert transforms based on Kerr micro-combs", Paper No. 11713-16, PW210-OE803-24, Next-Generation Optical Communication: Components, Sub-Systems, and Systems X, SPIE Photonics West, San Francisco CA March 6-11 (2021). DOI:10.1117/12.2584018
81. Mengxi Tan, X. Xu, J. Wu, A. Boes, T. G. Nguyen, S. T. Chu, B. E. Little, R. Morandotti, A. Mitchell, and David J. Moss, "Broadband photonic RF channelizer with 90 channels based on a soliton crystal microcomb", or "Photonic microwave and RF channelizers based on Kerr micro-combs", Paper No. 11685-22, PW210-OE106-49, Terahertz, RF, Millimeter, and Submillimeter-Wave Technology and Applications XIV, SPIE Photonics West, San Francisco CA March 6-11 (2021). DOI:10.1117/12.2584015

82. X. Xu, M. Tan, J. Wu, S. T. Chu, B. E. Little, R. Morandotti, A. Mitchell, B. Corcoran, D. Hicks, and D. J. Moss, "Photonic perceptron based on a Kerr microcomb for scalable high speed optical neural networks", IEEE Topical Meeting on Microwave Photonics (MPW), pp. 220-224. Matsue, Japan, November 24-26, 2020. Electronic ISBN:978-4-88552-331-1. DOI: 10.23919/MWP48676.2020.9314409
83. Mengxi Tan, Bill Corcoran, Xingyuan Xu, Andrew Boes, Jiayang Wu, Thach Nguyen, S.T. Chu, B. E. Little, Roberto Morandotti, Arnan Mitchell, and David J. Moss, "Ultra-high bandwidth optical data transmission with a microcomb", IEEE Topical Meeting on Microwave Photonics (MPW), pp. 78-82. Virtual Conf., Matsue, Japan, November 24-26, 2020. Electronic ISBN:978-4-88552-331-1. DOI: 10.23919/MWP48676.2020.9314476
84. M. Tan, X. Xu, J. Wu, R. Morandotti, A. Mitchell, and D. J. Moss, "RF and microwave high bandwidth signal processing based on Kerr Micro-combs", *Advances in Physics X*, VOL. 6, NO. 1, 1838946 (2021).
85. Mengxi Tan, Xingyuan Xu, Jiayang Wu, Thach G. Nguyen, Sai T. Chu, Brent E. Little, Roberto Morandotti, Arnan Mitchell, and David J. Moss, "Photonic Radio Frequency Channelizers based on Kerr Micro-combs and Integrated Micro-ring Resonators", JOSA Xiv.202010.0002.
86. Mengxi Tan, Xingyuan Xu, David Moss "Tunable Broadband RF Photonic Fractional Hilbert Transformer Based on a Soliton Crystal Microcomb", Preprints, DOI: 10.20944/preprints202104.0162.v1
87. Mengxi Tan, X. Xu, J. Wu, T. G. Nguyen, S. T. Chu, B. E. Little, R. Morandotti, A. Mitchell, and David J. Moss, "Orthogonally polarized Photonic Radio Frequency single sideband generation with integrated micro-ring resonators", *Journal of Semiconductors* <background-color:#FFCC66;buvertical-align:super;>42</background-color:#FFCC66;buvertical-align:super;> (4), 041305 (2021). DOI: 10.1088/1674-4926/42/4/041305.
88. X. Xu, *et al.*, "Photonic perceptron based on a Kerr microcomb for scalable high speed optical neural networks", *Laser and Photonics Reviews*, vol. 14, no. 8, 2000070, 2020.
89. X. Xu, *et al.*, "11 TOPs photonic convolutional accelerator for optical neural networks", *Nature* **589**, 44–51. 2021.
90. B. Corcoran, M. Tan, X. Xu, A. Boes, J. Wu, T. G. Nguyen, S. T. Chu, B. E. Little, R. Morandotti, A. Mitchell, and D. J. Moss, "Ultra-dense optical data transmission over standard fibre with a single chip source," *Nature Communications*, vol. 11, no. 1, pp. 2568, 2020/05/22, 2020.
91. J. Wu, X. Xu, T. G. Nguyen, S. T. Chu, B. E. Little, R. Morandotti, A. Mitchell, and D. J. Moss, "RF Photonics: An Optical Microcombs' Perspective," *IEEE J. Sel. Top. Quantum Electron.*, vol. 24, no. 4, pp. 6101020, Jul-Aug. 2018. DOI: 10.1109/JSTQE.2018.2805814.
92. T. G. Nguyen *et al.*, "Integrated frequency comb source-based Hilbert transformer for wideband microwave photonic phase analysis," *Opt. Express*, vol. 23, no. 17, pp. 22087-22097, Aug. 2015.
93. X. Xu, J. Wu, M. Shoeiby, T. G. Nguyen, S. T. Chu, B. E. Little, R. Morandotti, A. Mitchell, and D. J. Moss, "Reconfigurable broadband microwave photonic intensity differentiator based on an integrated

- optical frequency comb source," *APL Photonics*, vol. 2, no. 9, 096104, Sep. 2017.
94. X. Xu, M. Tan, J. Wu, R. Morandotti, A. Mitchell, and D. J. Moss, "Microcomb-based photonic RF signal processing", *IEEE Photonics Technology Letters*, vol. 31 no. 23 1854-1857, 2019.
95. X. Xu, *et al.*, "Broadband RF channelizer based on an integrated optical frequency Kerr comb source," *Journal of Lightwave Technology*, vol. 36, no. 19, pp. 4519–4526, 2018.
96. X. Xu, *et al.*, "Continuously tunable orthogonally polarized RF optical single sideband generator based on micro-ring resonators," *Journal of Optics*, vol. 20, no. 11, 115701. 2018.
97. X. Xu, *et al.*, "Orthogonally polarized RF optical single sideband generation and dual-channel equalization based on an integrated microring resonator," *Journal of Lightwave Technology*, vol. 36, no. 20, pp. 4808–4818. 2018.
98. X. Xu, *et al.*, "Photonic microwave true time delays for phased array antennas using a 49 GHz FSR integrated optical micro-comb source," *Photonics Res*, vol. 6, no. 5, pp. B30-B36, 2018.
99. X. Xu, *et al.*, "Advanced adaptive photonic RF filters with 80 taps based on an integrated optical micro-comb source," *Journal of Lightwave Technology*, vol. 37, no. 4, pp. 1288–1295, 2019.
100. X. Xu, *et al.*, "Broadband microwave frequency conversion based on an integrated optical micro-comb source", *Journal of Lightwave Technology*, vol. 38 no. 2, pp. 332–338, 2020.
101. M. Tan, *et al.*, "Photonic RF and microwave filters based on 49GHz and 200GHz Kerr microcombs", *Optics Comm.* vol. 465,125563, Feb. 22. 2020.
102. X. Xu, *et al.*, "Broadband photonic RF channelizer with 90 channels based on a soliton crystal microcomb", *Journal of Lightwave Technology*, Vol. 38, no. 18, pp. 5116 - 5121, 2020. doi: 10.1109/JLT.2020.2997699.
103. X. Xu, *et al.*, "Photonic RF and microwave integrator with soliton crystal microcombs", *IEEE Transactions on Circuits and Systems II: Express Briefs*, vol. 67, no. 12, pp. 3582–3586, 2020. DOI:10.1109/TCSII.2020.2995682.
104. X. Xu, *et al.*, "Photonic RF phase-encoded signal generation with a microcomb source", *Journal of Lightwave Technology*, vol. 38, no. 7, pp. 1722–1727, 2020.
105. X. Xu, *et al.*, "High performance RF filters via bandwidth scaling with Kerr micro-combs," *APL Photonics*, vol. 4, no. 2, pp. 026102. 2019.
106. M. Tan, *et al.*, "Microwave and RF photonic fractional Hilbert transformer based on a 50 GHz Kerr micro-comb", *Journal of Lightwave Technology*, vol. 37, no. 24, pp. 6097–6104, 2019.
107. M. Tan, *et al.*, "RF and microwave fractional differentiator based on photonics", *IEEE Transactions on Circuits and Systems: Express Briefs*, vol. 67, no.11, pp. 2767–2771, 2020. DOI:10.1109/TCSII.2020.2965158.
108. M. Tan, *et al.*, "Photonic RF arbitrary waveform generator based on a soliton crystal micro-comb source", *Journal of Lightwave Technology*, vol. 38, no. 22, pp. 6221-6226, Oct 22. 2020. DOI: 10.1109/JLT.2020.3009655.

109. M. Tan, X. Xu, J. Wu, R. Morandotti, A. Mitchell, and D. J. Moss, "RF and microwave high bandwidth signal processing based on Kerr Micro-combs", *Advances in Physics X*, VOL. 6, NO. 1, 1838946 (2021).
110. X. Xu, et al., "Advanced RF and microwave functions based on an integrated optical frequency comb source," *Opt. Express*, vol. 26, no. 3, pp. 2569-2583, Feb. 2018.
111. Xu, X., et al., Photonic microwave true time delays for phased array antennas using a 49 GHz FSR integrated
112. Alberto Della Torre, Milan Sinobad, Remi Armand, Barry Luther-Davies, Pan Ma, Stephen Madden, Arnan Mitchel, David J. Moss, Jean-Michel Hartmann, Vincent Reboud, Jean-Marc Fedeli, Christelle Monat, Christian Grillet, "Mid-infrared supercontinuum generation in a low-loss germanium-on-silicon waveguide", *APL Photonics*, vol. 6, 016102 (2021); doi: 10.1063/5.0033070.
113. Milan Sinobad, Alberto Della Torre, Remi Armand, Barry Luther-Davies, Pan Ma, Stephen Madden, Arnan Mitchell, David J. Moss, Jean-Michel Hartmann, Jean-Marc Fedeli, Christelle Monat, and Christian Grillet, "Mid-infrared supercontinuum generation in silicon-germanium all-normal dispersion waveguides", *Optics Letters*, vol. 45, Issue 18, 5008–5011 (2020). DOI: 10.1364/OL.402159.
114. Milan Sinobad, Alberto Della Torre, Barry Luther-Davis, Pan Ma, Stephen Madden, Arnan Mitchell, David J. Moss, Jean-Michel Hartmann, Jean-Marc Fédéli, Christelle Monat and Christian Grillet, "High coherence at  $f$  and  $2f$  of a mid-infrared supercontinuum in a silicon germanium waveguide", *IEEE Journal of Selected Topics in Quantum Electronics*, vol. 26, Issue 2, 8201008 (2020).
115. Milan Sinobad, Alberto Della Torre, Barry Luther-Davis, Pan Ma, Stephen Madden, Sukanta Debbarma, Khu Vu, David J. Moss, Arnan Mitchell, Regis Orobtcchouk, Jean-Marc Fedeli, Christelle Monat, and Christian Grillet, "Dispersion trimming for mid-infrared supercontinuum generation in a hybrid chalcogenide/silicon-germanium waveguide", *Journal of the Optical Society of America B*, vol. 36, Issue 2, A98-A104 (2019).
116. Milan Sinobad, Christelle Monat, Barry Luther-Davies, Pan Ma, Stephen Madden, David J. Moss, Arnan Mitchell, David Allieux, Regis Orobtcchouk, Salim Boutami, Jean-Michel Hartmann, Jean-Marc Fedeli, Christian Grillet, "High brightness mid-infrared octave spanning supercontinuum generation to  $8.5\mu\text{m}$  in chip-based Si-Ge waveguides", *Optica*, Vol. 5, Issue 4, 360–366 (2018).
117. N. Singh, D. D. Hudson, Y. Yu, C. Grillet, S. D. Jackson, A. Casas-Bedoya, A. Read, P. Atanackovic, S. G. Duvall, S. Palomba, B. Luther-Davies, S. Madden, D. J. Moss, and B. J. Eggleton, "Midinfrared supercontinuum generation from 2 to  $6\mu\text{m}$  in a silicon nanowire," *Optica*, vol. 2, no. 9, pp. 797–802, 2015.
118. L. Carletti, P. Ma, B. Luther-Davies, D. Hudson, C. Monat, S. Madden, M. Brun, S. Ortiz, S. Nicoletti, D. J. Moss, and C. Grillet, "Nonlinear optical properties of SiGe waveguides in the mid-infrared", *Optics Express*, Vol. 23, Issue 7, pp. 8261–8271 (2015).

## Figures

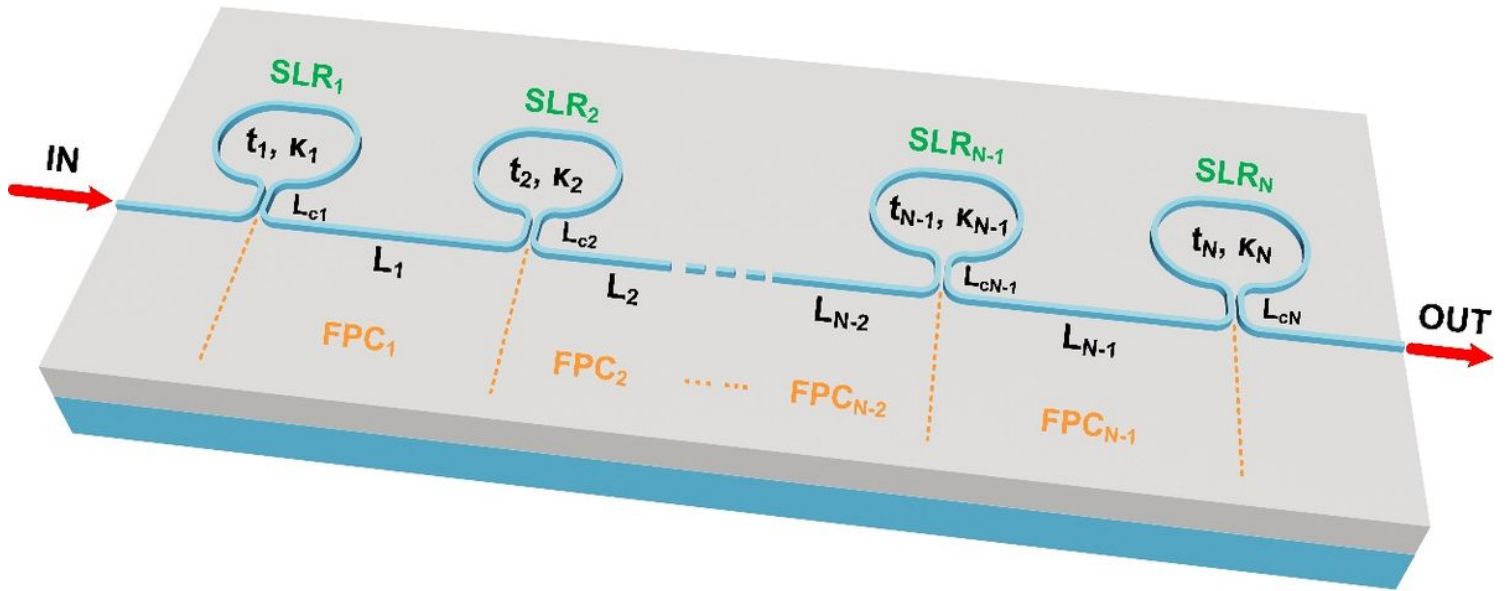


**Figure 1**

Schematic configuration of integrated CSLR resonator made up of  $N$  cascaded SLRs ( $SLR_1, SLR_2, \dots, SLR_N$ ).  $FPC_i$  ( $i = 1, 2, \dots, N-1$ ) are the FP cavities formed by  $SLR_i$  and  $SLR_{i+1}$ , respectively. The definitions of  $t_i$  ( $i = 1, 2, \dots, N$ ),  $k_i$  ( $i = 1, 2, \dots, N$ ),  $L_{c_i}$  ( $i = 1, 2, \dots, N$ ), and  $L_i$  ( $i = 1, 2, \dots, N-1$ ) are given in Table I.

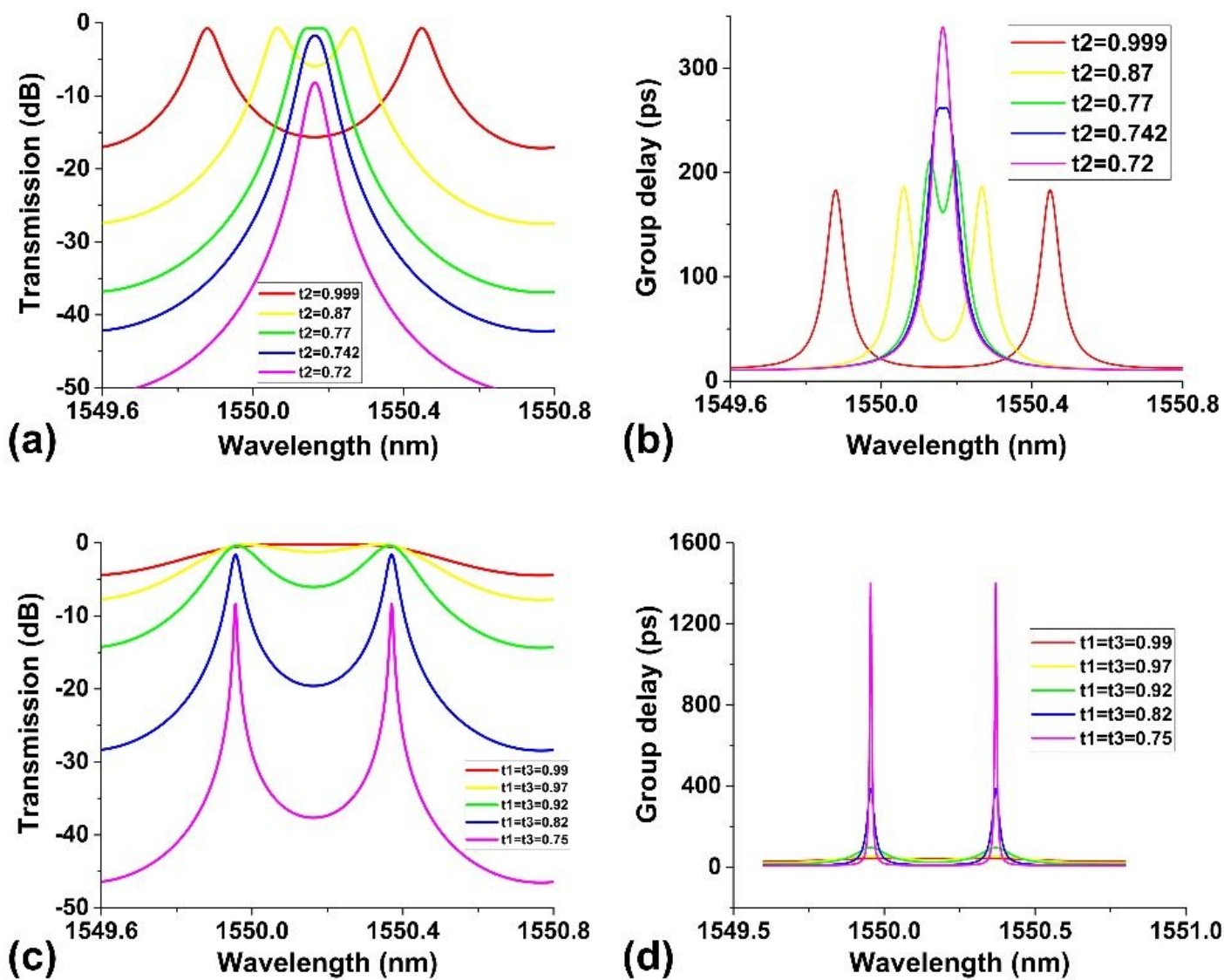


Figure 2

(a) Calculated power transmission spectra of the CSLR resonator (N = 3) for various  $t_2$  when  $t_1 = t_3 = 0.87$ . (b) Calculated group delay spectra of the CSLR resonator (N = 3) for various  $t_2$  when  $t_1 = t_3 = 0.87$ . (c) Calculated power transmission spectra of the CSLR resonator (N = 3) for various  $t_1 = t_3$  when  $t_2 = 0.97$ . (d) Calculated group delay spectra of the CSLR resonator (N = 3) for various  $t_1 = t_3$  when  $t_2 = 0.97$ .

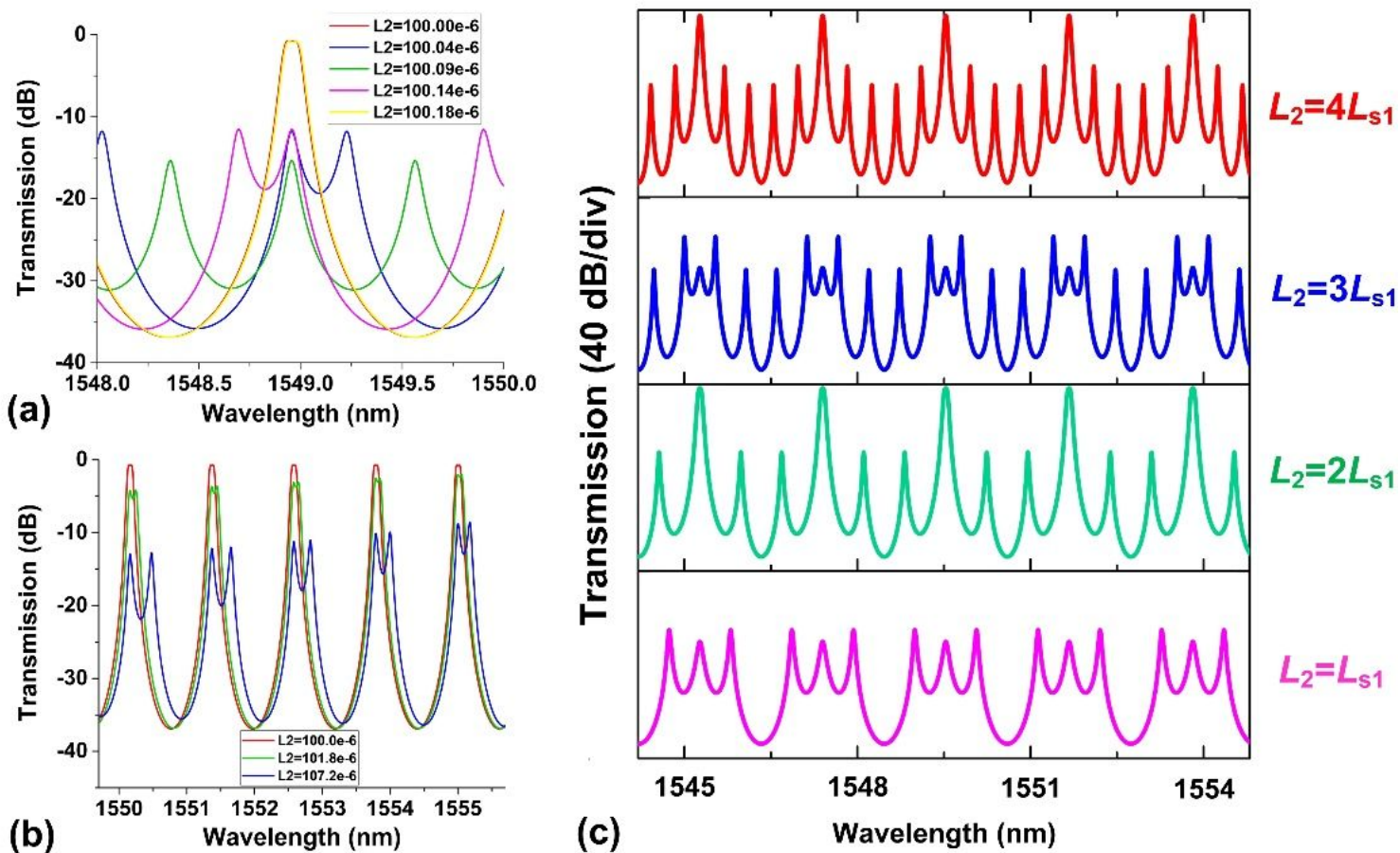


Figure 3

(a) Calculated power transmission spectra of the CSLR resonator ( $N = 3$ ) for various  $L_2$  from  $100.00 \mu\text{m}$  to  $100.18 \mu\text{m}$  when  $L_1 = 100.00 \mu\text{m}$ . (b) Calculated power transmission spectra of the CSLR resonator ( $N = 3$ ) for various  $L_2$  from  $100.0 \mu\text{m}$  to  $107.2 \mu\text{m}$  when  $L_1 = 100.0 \mu\text{m}$ . (c) Calculated power transmission spectra of the CSLR resonator ( $N = 3$ ) for various  $L_2$  from  $L_{s1}$  to  $4L_{s1}$  when  $L_1 = 0 \mu\text{m}$ .

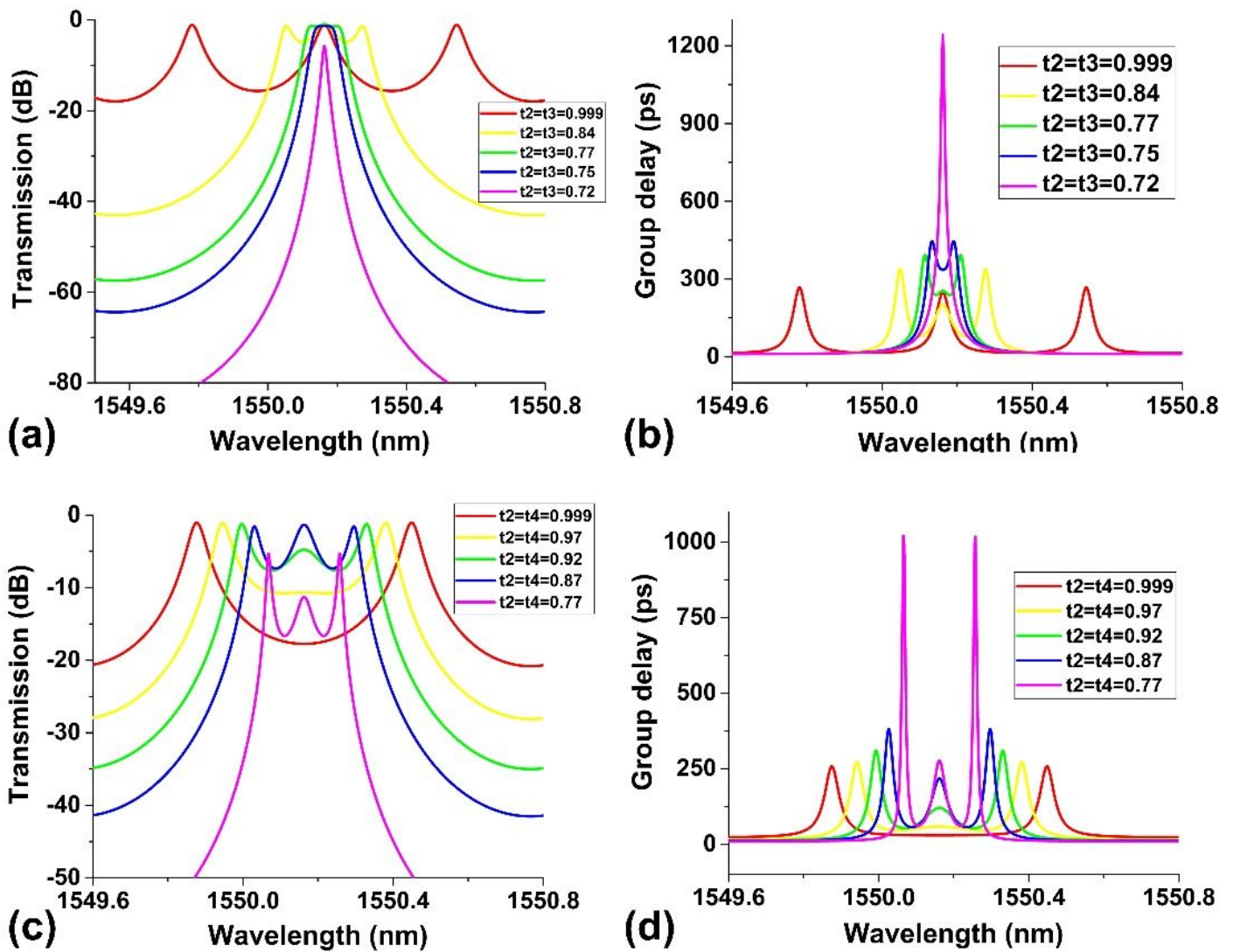
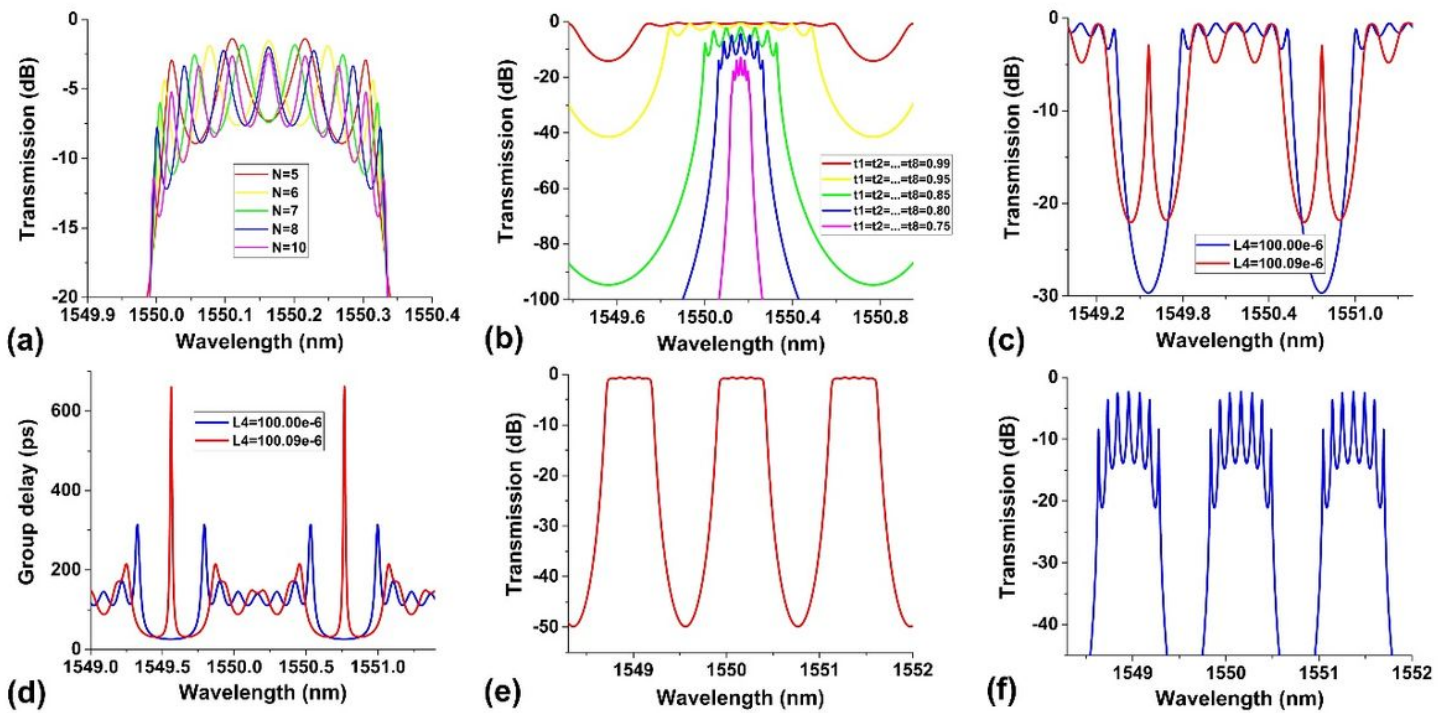


Figure 4

(a) Calculated power transmission spectra of the CSLR resonator (N = 4) for various  $t_2 = t_3$  when  $t_1 = t_4 = 0.87$ . (b) Calculated group delay spectra of the CSLR resonator (N = 4) for various  $t_2 = t_3$  when  $t_1 = t_4 = 0.87$ . (c) Calculated power transmission spectra of the CSLR resonator (N = 4) for various  $t_2 = t_4$  when  $t_1 = t_3 = 0.85$ . (d) Calculated group delay spectra of the CSLR resonator (N = 4) for various  $t_2 = t_4$  when  $t_1 = t_3 = 0.85$ .



**Figure 5**

(a) Calculated power transmission spectra of the CSLR resonator for various  $N$  when  $t_1 = t_2 = \dots = t_N = 0.85$ . (c) Calculated power transmission spectra of the CSLR resonator ( $N = 8$ ) for different  $t_1 = t_2 = \dots = t_8$ . (c) Calculated power transmission spectra of the CSLR resonator ( $N = 8$ ) for enhanced light trapping. (d) Calculated group delay spectra of the CSLR resonator ( $N = 8$ ) in (c). (e) Calculated power transmission spectra of 8th-order Butterworth filter based on the CSLR resonator ( $N = 8$ ). (f) Calculated power transmission spectra of the CSLR resonator ( $N = 8$ ) with multiple transmission peaks.

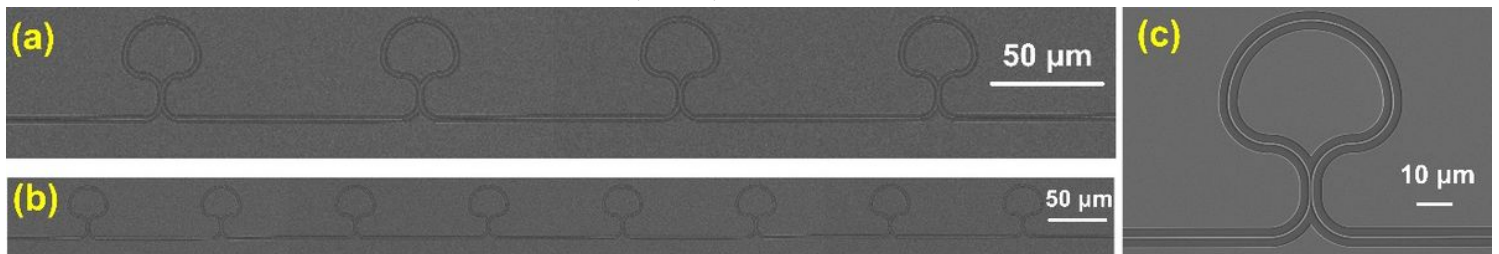


**Figure 6**

(a) Micrograph for one of the fabricated CSLR resonators with four SLRs. (b) Micrograph for one of the fabricated CSLR resonators with eight SLRs. (c) Zoom-in micrograph for the SLR.

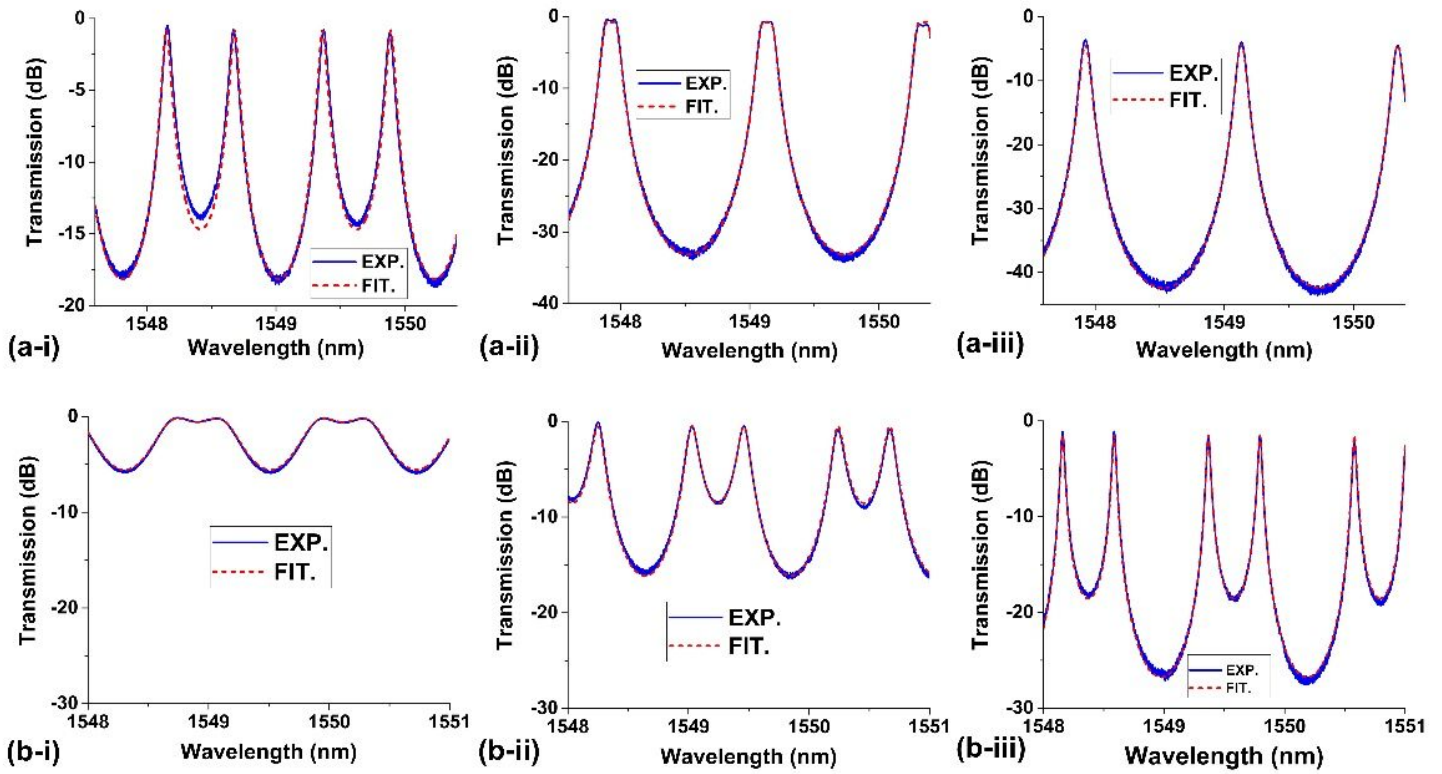


Figure 7

(a) Measured (solid curve) and fit (dashed curve) transmission spectra of three fabricated CSLR resonators ( $N = 3$ ) with different  $L_{c2}$ . (b) Measured (solid curve) and fit (dashed curve) transmission spectra of three fabricated CSLR resonators ( $N = 3$ ) with different  $L_{c1} = L_{c3}$ .

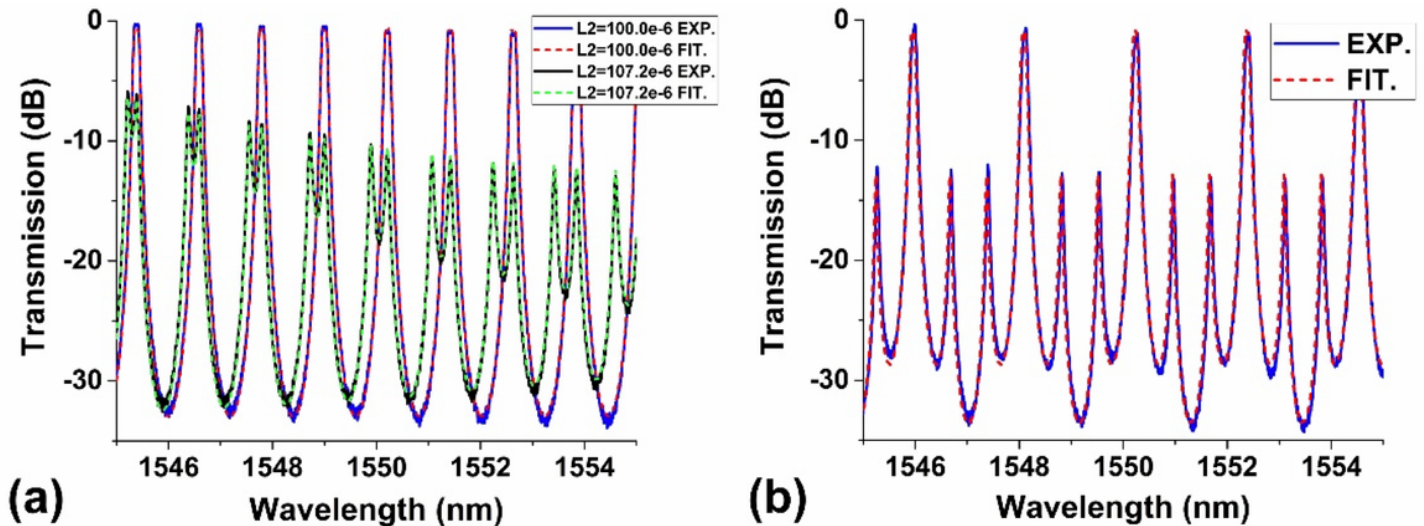
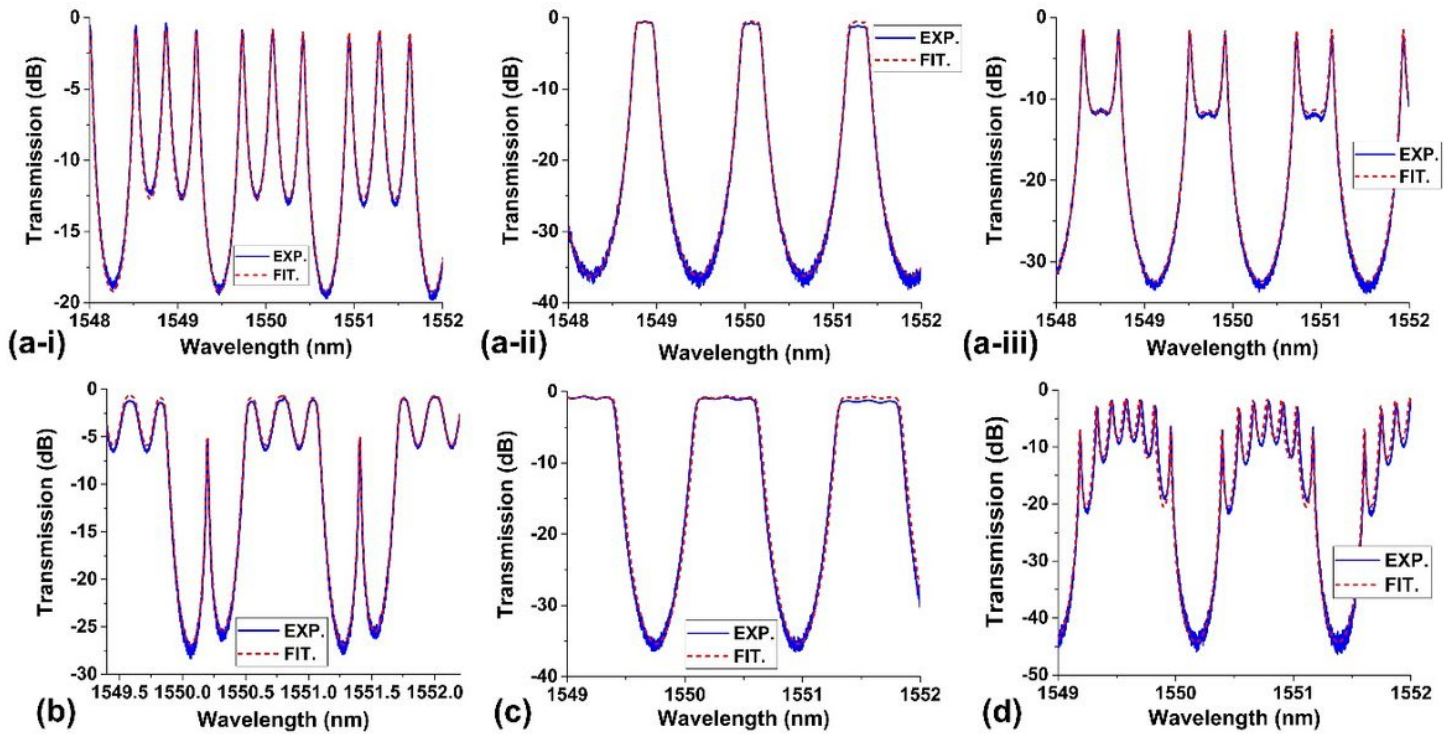


Figure 8

(a) Measured (solid curve) and fit (dashed curve) transmission spectra of two fabricated CSLR resonators ( $N = 3$ ) with different  $L_2 = 100.0 \mu\text{m}$  and  $107.2 \mu\text{m}$ . (b) Measured (solid curve) and fit (dashed curve) transmission spectra of a fabricated CSLR resonator ( $N = 3$ ) with  $L_1' = 0 \mu\text{m}$  and  $L_2 = 295.33 \mu\text{m}$ .



**Figure 9**

(a) Measured (solid curve) and fit (dashed curve) transmission spectra of three fabricated CSLR resonators ( $N = 4$ ) with different  $L_{ci}$  ( $i = 1, 2, 3, 4$ ). (b) Measured (solid curve) and fit (dashed curve) transmission spectra of a fabricated CSLR resonator ( $N = 8$ ) for enhanced light trapping. (c) Measured (solid curve) and fit (dashed curve) transmission spectra of a fabricated CSLR resonator ( $N = 8$ ) with flat-top filter shape. (d) Measured (solid curve) and fit (dashed curve) transmission spectra of a fabricated CSLR resonator ( $N = 8$ ) with multiple split resonances.